

Reconstruction of Natural Visual Scenes from Neural Spikes with Deep Neural Networks

Yichen Zhang, Shanshan Jia, Yajing Zheng, Zhaofei Yu, Yonghong Tian,
Tiejun Huang, Jian K. Liu

Abstract

Neural coding is one of the central questions in systems neuroscience for understanding how the brain processes stimulus from the environment, moreover, it is also a cornerstone for designing algorithms of brain-machine interface, where decoding incoming stimulus is needed for better performance of physical devices. Traditionally, the neural signal of interest for decoding visual scenes has been focused on fMRI data. However, our visual perception operates in a fast time scale of millisecond in terms of an event termed neural spike. So far there are few studies of decoding by using spikes. Here we fulfill this aim by developing a novel decoding framework based on deep neural networks, named spike-image decoder (SID), for reconstructing natural visual scenes, including static images and dynamic videos, from experimentally recorded spikes of a population of retinal ganglion cells. The SID is an end-to-end decoder with one end as neural spikes and the other end as images, which can be trained directly such that visual scenes are reconstructed from spikes in a highly accurate fashion. In addition, we show that SID can be generalized to arbitrary images by using image datasets of MNIST, CIFAR10, and CIFAR100. Furthermore, with a pre-trained SID, one can decode any dynamic videos, with the aid of an encoder, to achieve real-time encoding and decoding visual scenes by spikes. Altogether, our results shed new light on neuromorphic computing for artificial visual systems, such as event-based visual cameras and visual neuroprostheses.

Y. Zhang, S. Jia, Y. Zheng, Z. Yu, Y. Tian, T. Huang are with the National Engineering Laboratory for Video Technology, School of Electronics Engineering and Computer Science, Peking University, Beijing 100871, China, and also with Peng Cheng Laboratory, Shenzhen 518055, China (e-mail: zhang-yc16@pku.edu.cn, jssl100@126.com, zyj061@pku.edu.cn, yuzf12@pku.edu.cn, yhtian@pku.edu.cn, tjhuang@pku.edu.cn).

J. K. Liu is with the Centre for Systems Neuroscience, Department of Neuroscience, Psychology and Behaviour, University of Leicester, Leicester LE1 7HA, U.K, and also with Peng Cheng Laboratory, Shenzhen 518055, China (e-mail: jian.liu@leicester.ac.uk).

I. INTRODUCTION

In everyday life, various types of sensory information are processed by our brain through different sensory modalities, as a result, one has to conduct certain behaviors as reactions. Neuronal networks in the brain, then, play an essential role in efficient and powerful computation where a sequence of input-output mappings is carried out by single and networked neurons. At the level of the system, single neurons receive and response input stimuli by changing their membrane potentials to generate a sequence of fast events, termed neural spikes. Thus, spikes have been suggested as a fundamental element to represent input-output neural computation.

Such observations lead to a central question for systems neuroscience regarding the sensory system: how do neurons represent the input-output relationship between stimuli and their spikes [1], [2], [3]. This question, formulated as neural coding, consists of two essential parts, encoding, and decoding. For the visual system, it is to understand how visual scenes are represented by neural spiking activities, and how to decode neural spiking activities to reconstruct the given visual scenes.

The retina serves as a useful system to study these questions. Visual scenes are projected into the eyes, where the retinal network processes these inputs by a few types of neurons, but the only output neurons are the retinal ganglion cells (RGCs). Therefore, all information of visual scenes is encoded by RGCs that produce a sequence of action potentials or spikes, which are transmitted via the optic nerve to the downstream brain region. Essentially, visual scenes are represented by spikes of a population of RGCs. One expects that encoding and decoding of visual scenes from RGC spikes can be formulated into a closed form where computational models can be developed to set up a mapping between visual scenes and RGC spikes.

Indeed, much effort has been given to study the encoding part of RGCs. Various neuroscience mechanisms have been identified in understanding the retinal computation of visual scenes by its neurons and neural circuitry [4], [5], [6], [7], [8], [9], [10], [11]. In addition, for understanding the encoding principles of the retina, a number of models are developed based on different biophysical properties of neurons and neural circuits in the retina [12].

In contrast, decoding of RGC spikes to obtain essential information of visual scenes is processed by the downstream neurons from the lateral geniculate nucleus to the visual cortex, which involves feedbacks from the higher part of the cortex for cognition. As the retina does not receive these feedbacks, the RGC spikes can be thought as a minimal computational device to

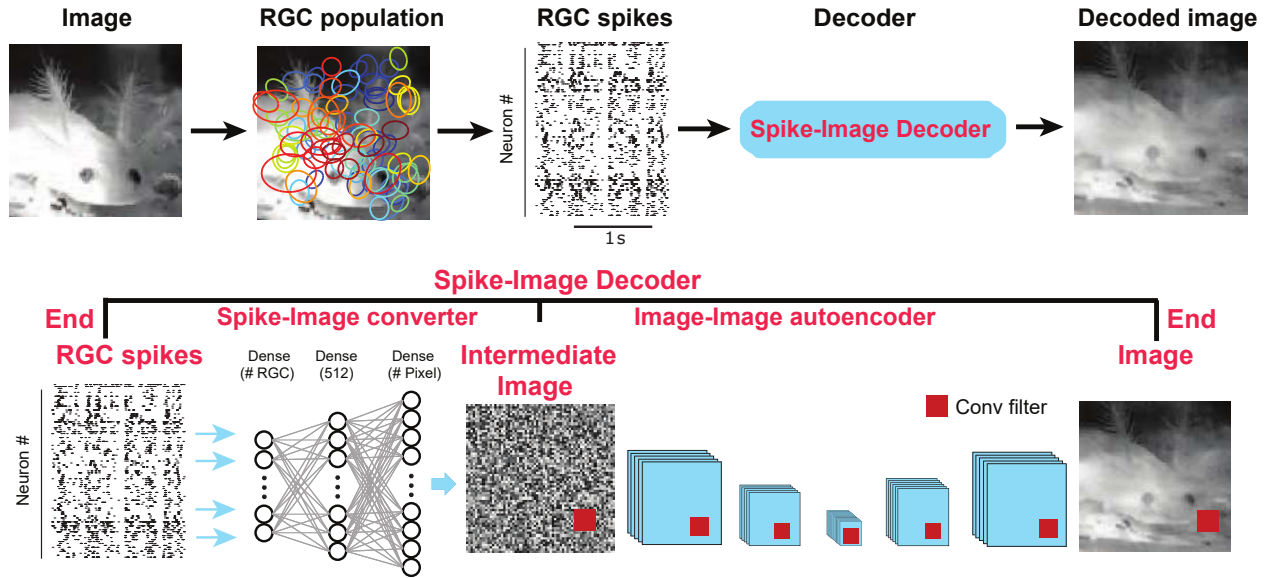


Fig. 1: Decoding visual scenes from neural spikes. (Top) Workflow of decoding visual scenes. Here a salamander swimming video was presented to a salamander retina to get a population of ganglion cells fired with a sequence of spikes. A population of spikes is used to train the SID model for the given video to get reconstructed visual scenes. The receptive fields of ganglion cells are mapped onto the image. Each colored circle is an outline of the receptive field. (Bottom) The SID is an end-to-end decoder with two stages: spike-image converter used to map the population of spikes to a pixel-level intermediate image, and image-image autoencoder to map every pixel to the target pixel in the desired image.

represent visual information as a whole. Therefore, it is suitable to develop a decoding model that can reconstruct visual scenes from the RGC spikes [13], [14]. In general, for a neuronal system, an ideal decoder should be able to read out and reconstruct stimulus from neural responses. The existing methods for visual scenes reconstruction are mainly divided into two types. The first one is to decode the stimulus category: choosing a stimulus according to neural responses, then classifying neural signals to find the corresponding stimulus in a candidate set [15]. The second type is reconstructing the original stimulus directly by using neural responses, i.e., obtaining every pixel of visual scenes from the neural signal. It is obvious that the second category is more challenging [16], [13].

Reconstruction of visual scenes has been studied over many years. The neural signals of

interest can be fMRI activities [17], [18], [16], [15], [19], neural spikes in the retina [20], [21], [14], [13] and lateral geniculate nucleus [22], neural calcium imaging data in V1 [23]. However, the decoding performance of current methods is rather low for natural scenes, in particular for dynamical videos, which can be seen from some examples of the videos reconstructed from fMRI data [16], [15].

For the retina, one would expect to decode visual scenes by using the spiking responses of a population of RGCs in a complete way as these spikes are the only outputs of the eyes. Decoding of visual scenes, at least for natural images, is possible when sampling the whole image with a number of RGCs [13], or when a few thousands of simulated RGCs are used [21]. Yet, it remains unclear how to deal with the dynamic natural scenes, where the temporal complexity of stimulus information has a strong coupling with the temporal adaption of neurons [24].

In this study, we propose such a decoding approach, termed spike-image decoder (SID), that performs an end-to-end decoding process from neural spikes to visual scenes, based on a model of deep learning neural network. The proposed SID can achieve state-of-the-art performance than previous studies for reconstructing natural visual scenes, including both static images and dynamic videos, from spikes of a population of RGCs recorded simultaneously in the isolated animal retina. The workflow of the SID is illustrated in Fig. 1. With a setup of the multi-electrode array, a large population of RGCs can be recorded simultaneously, and their spikes can be extracted. Then, a spike-image converter based on a neural network is used to map and up-sample spikes of every RGC to intermediate images at the pixel level. After that, an autoencoder-type deep learning neural network is applied to spike-based intermediate images to match original stimulus images for every pixel.

Essentially, the SID has two stages with one as spike-image converter and another one as image-image autoencoder. Most of the previous studies focused on the first stage, such that spikes are directly mapped to obtain the image pixels, where, traditionally, a decoder can be optimized by some statistical models in a linear or nonlinear fashion [17], [18], [16], [20], [14], [13], [22]. A recent study trained a separate autoencoder network as the second stage to enhance the quality of images [21], which essentially employed a similar network dedicated for image denoising and enhancement [25]. Here, we systematically tested different training approaches of neural networks from spikes to images, and found the SID can achieve similar performance for static images across three types of loss functions, but for dynamic videos, the direct training from spikes to images shows an outstanding performance.

We tested the performance of SID on experimentally recorded RGCs spikes, and found it can obtain state-of-the-art performance for the reconstruction of natural visual scenes of static images and dynamic video. Furthermore, we show that the computational ability of SID can be generalized to arbitrary visual scenes with the aid of an encoding model that can simulate spikes for any given images. By using image datasets of MNIST, CIFAR10, and CIFAR100, the SID can reconstruct natural images with high precision. In addition, with a pre-trained SID model, one can reconstruct any given video scenes to realize real-time encoding and decoding dynamic visual scenes as an artificial vision system.

II. METHODS

A. Spike-image decoder

Traditionally, it has been shown that deep neural networks can extract low-level features in earlier layers, and more semantic features in later layers, which is similar to the information processing of the visual cortex in the brain [26]. Here we use a similar deep neural network to reconstruct natural scenes from the retinal spikes. Our decoding model consists of two parts: 1) spike-to-image converter and 2) image-to-image autoencoder. The spike-to-image converter is able to map every spike to every pixel to get intermediate images, which plays a role of nonlinear up-sampling, and the image-to-image autoencoder is used to match all pixels to those of the target images of visual scenes.

1) *Model architecture*: Given an input image \mathbf{I} , it will trigger a response $s = \{s_1, s_2 \dots s_n\}$ on the retinal ganglion cells (RGCs), here we use rate coding such that s_i represents the spike count of each RGC within a time bin depending on the sampling rate of visual scenes. As in experimental recordings, a typical 30 Hz refreshing rate is used, so the time bin is about 33 ms. Then the triggered responses are first fed into the spike-to-image converter, which is a three-layer fully-connected neural network. The network outputs an intermediate image $\mathbf{O}_1 = f_1(\mathbf{s})$ from RGC responses. Then the image-to-image autoencoder takes the intermediate image as input, and is able to denoise and map it to match the target image, so one can get a more clear and refining reconstruction result $\mathbf{O}_2 = f_2(\mathbf{O}_1)$. These two parts are all implemented with deep neural networks, so end-to-end training can be used to train both networks.

Three different ways of defining loss function were explored in this study. In the first one, one can use a multi-task loss function to make sure both stages have the capability to decode natural scenes from spikes, so that we can get a high quality reconstruction result from our decoding

model. Here, λ_1 and λ_2 are weights of these two parts mean square error loss, $\mathbf{L}_1 : Loss = \lambda_1 \|\mathbf{O}_1 - \mathbf{I}\| + \lambda_2 \|\mathbf{O}_2 - \mathbf{I}\|$. In the second one, we optimize each stage of decoding separately such that $\mathbf{L}_2 : (Loss_1 = \lambda_1 \|\mathbf{O}_1 - \mathbf{I}\|, Loss_2 = \lambda_2 \|\mathbf{O}_2 - \mathbf{I}\|)$. The third one uses one loss for the whole process of two stages as following: $\mathbf{L}_3 : Loss = \lambda \|\mathbf{O} - \mathbf{I}\|$, where there is only one image output \mathbf{O} as the final reconstruction to compare the target image such that one error signal stays in both stages. In this way, we found that the intermediate image is like noise without visible structure as in Fig. 1. Three loss functions are compared in details.

2) *Spike-to-image converter*: The spike-to-image converter is a three-layer fully-connected neural network. The first layer receives spikes of all RGCs as input such that the number of neurons of the first layer is matched to the number of RGCs used. The second layer is a hidden layer, which consists of 512 neurons. ReLU is used as an activation function of the hidden layer. The output layer has the same number of neurons as the pixel number of the input image, in our case, 4096 neurons are used since all stimulus images are in 64*64 pixels. ReLU as activation function is used for the third layer, and we can get all pixel values of intermediate images from this output layer. During training, batch normalization is used to achieve better performance and dropout is used to deal with overfitting.

3) *Image-to-image autoencoder*: The image-to-image autoencoder is a typical deep autoencoder based on convolutional neural network, where the whole information processing procedure can be split into two phases. In the first phase, convolution and down-sampling are used to process and decrease the size of the input image. After this phase, the most important components of the input image are kept, and those noise and redundant contents are filtered. In the second phase, convolution and up-sampling are used to process the image, which recovers the texture of the down-sampled image while increasing the size of the down-sampled image. Batch normalization and dropout are also used during training.

B. Experimental RGC data

Our decoder was used to reconstruct natural visual scenes, including both static images and dynamic videos, from spikes of a population of RGCs recorded simultaneously in isolated retinas of salamanders. Experimental details can be found in previous studies [27], [28], and datasets of spikes recorded and stimulus images and movies used in this study can be found publicly [27].

1) *Image stimulus*: The static images were taken from a public dataset [27], including 300 natural images with a size of 64*64 pixels. Briefly, each image covers 1920*1920 μm area on

the retina, in which there are 80 RGCs recorded. Each individual image was presented in 200 ms and then followed by an 800 ms empty display in a pseudo-random sequence. For each image to each RGC, the number of spike count during 300 ms in one trail was collected. In addition, we averaged the spike counts among 13 trails for each image. Finally, we got the spike counts of a population of 80 RGCs for one image as the input data for reconstruction. Among all 300 images, 270 images were used to train the decoder model and the remaining 30 images were used as the test set.

2) *Video stimulus*: The same dataset in [27] also provides video data consisted of salamander swimming which includes 1800 frames. Each frame covered a total area of $2700 \times 2700 \mu\text{m}$ on the retina with a spatial resolution of 360×360 pixels, in which 90 RGCs responses were collected. A segment of the video was presented at a frame rate of 30 Hz. For the recorded responses of each RGC, one can bin that into 33 ms that is same with the presentation time of each frame. As a result, a spike train was collected with 1800 counts for each RGC in response to the video. Finally, for the population of RGCs, a 90×1800 spike count matrix will be used to reconstruct the video. To train the decoder model, we randomly selected 1620 frames from the video as a training set and the remaining frames as a test set. In this way, the strong temporal correlation within the video can be washed out.

C. Simulated RGC data

To test our SID model for any arbitrary visual scenes, we used a simple encoder based on the typical linear-nonlinear model [29], [28] to simulate neural responses of a populating of RGCs. For comparison, the encoding model is based on the same experimental retinal data used for the analysis of the video. The linear filters are based on the receptive fields of a population of 90 RGCs obtained with white noise analysis [27] fitted with a 2D Gaussian for each cell. With the given natural scene stimulus (a static image or a frame of dynamic video), each cell did a linear computation on pixels within its receptive field, and generated a spike count for this stimulus after a threshold-linear nonlinearity. All these simulated spike counts (modeled responses of 90 RGCs) were then fed into our SID model to reconstruct natural scene stimulus.

With this retinal encoding model, one can simulate RGC responses under any given stimuli. In this study, simulations can be done on three popular image datasets, MNIST, CIFAR10, and CIFAR100. MNIST is a dataset of handwritten digits that consists of a training set of 60,000 examples and a testing set of 10,000 examples. CIFAR10 and CIFAR100 are datasets used for

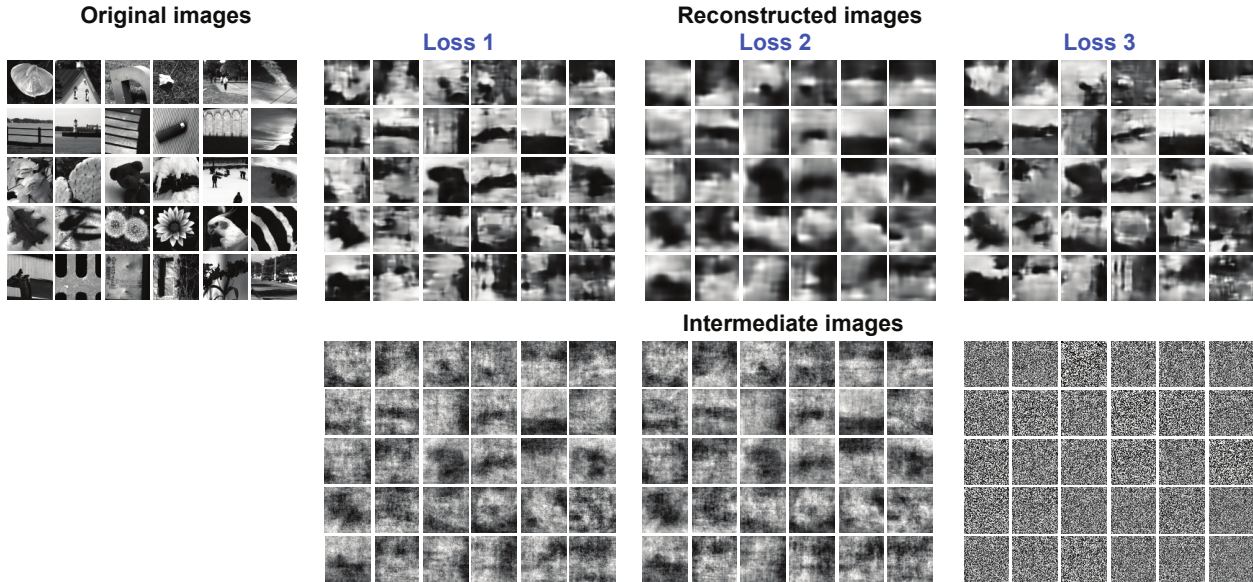


Fig. 2: Reconstructed natural images from experimental RGC spikes with different loss functions. (Left) original stimulus images in the test data. (Right) final reconstructed images (top) and intermediate images (bottom) from RGC spikes with three loss functions. Different losses can lead to quite different intermediate images, in particular, they are noise images in Loss 3.

image classification, consisting of 60,000 color images in 10 and 100 classes respectively. There are 50,000 training images and 10,000 testing images in both of CIFAR10 and CIFAR100. All images were first resized to the size of 64*64 pixels, which is comparable to our retinal experimental data. Then, as described above, the encoding model was used to encode images into RGC spikes, which can be tested for our SID model to reconstruct stimulus images from simulated RGC spikes.

Similarly, for comparison, dynamic videos were also used for testing the SID. With the same encoding model, we used the same movie chips from the fMRI decoding experiments [16], and obtained a set of RGC spiking responses similar to the biological data. Then the SID model pre-trained with CAFAR10 dataset was used to decode these dynamic videos directly.

Finally, we implemented real-time coding of arbitrary visual scenes by embedding our models into the power-efficient AI computing device, here NVIDIA Jetson TX2, which is built around a 256-core NVIDIA Pascal GPU. In order to better take advantage of the GPU to accelerate the computation, we combined the image-spike encoding process into the decoding neural networks.

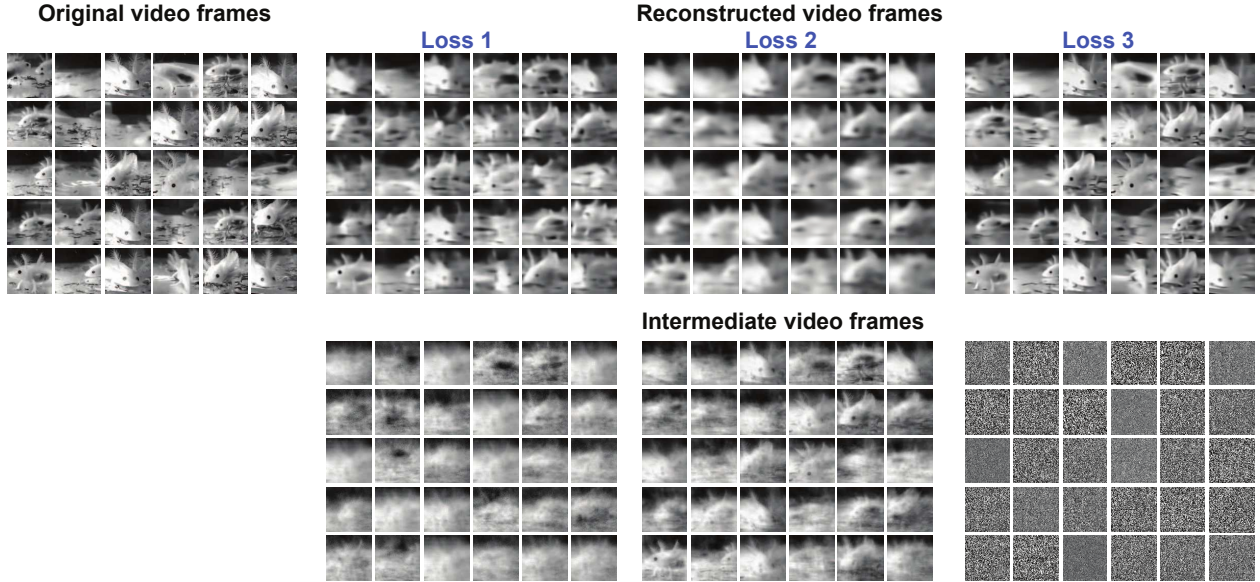


Fig. 3: Reconstructed dynamic video from experimental RGC spikes with different loss functions. Similar to Fig. 2, except that here are some random frames of a continuous video.

TABLE I: Quantified performance of reconstructed images measured by MSE, PSNR and SSIM for experimental RGC spikes with three different loss functions. The best values are marked in bold.

| Loss | Reconstruction | Image | | | Video | | |
|----------------------|-----------------------------------|---------------|----------------|---------------|---------------|----------------|---------------|
| | | MSE | PSNR | SSIM | MSE | PSNR | SSIM |
| L₁ | Intermediate O₁ | 0.0412 | 20.0238 | 0.1454 | 0.0289 | 21.6517 | 0.2732 |
| | Final O₂ | 0.0327 | 21.1262 | 0.2779 | 0.0156 | 25.0245 | 0.4953 |
| L₂ | Intermediate O₁ | 0.0362 | 20.5706 | 0.1867 | 0.0164 | 24.5617 | 0.4569 |
| | Final O₂ | 0.0329 | 21.0605 | 0.2873 | 0.0156 | 24.7261 | 0.4604 |
| L₃ | Intermediate O₁ | 0.3802 | 10.4114 | 0.0006 | 0.4328 | 10.4352 | 0.0014 |
| | Final O₂ | 0.0345 | 20.9736 | 0.2828 | 0.0079 | 29.7626 | 0.7121 |

In the real-time coding system, we can choose the input files such as image or video from the embedded device, or directly read the inputs, i.e. a real-time video, from a camera. However, as our SID was pre-trained with 64×64 pixels as input stimulus and target output, the resolution is not very high such that it misses the fine detailed structure of visual scenes. Therefore, based on the pre-trained SID, we cropped the inputs stimulus into several patches with 64×64 pixels, and then we joined the decoding results after sending these data as a batch into the model

simultaneously. Considering the GPU processing speed as well as the resolution, we cropped the input frames as 5×5 patches, such that the resolution of input images and decoding results can be increased to 320×320 in a real-time fashion. Higher resolution with real-time speed can be further achieved depending on the hardware used for this artificial vision system.

The reconstruction results of the same videos as a previous study [16] and our real-time video decoding are available on the web page (<https://sites.google.com/site/jiankliu>).

III. RESULTS

To test the capability of our SID model for the reconstruction of visual scenes, we first use our decoding model to reconstruct natural stimulus from biological experimental data that consists of a population of RGCs recorded in salamander retina triggered by natural images and videos. To further test the generalization capability of our model, a set of simulated experiments with the encoding model are conducted, in which we reconstruct stimulus images of MNIST, CIFAR10, and CIFAR100 from modeled spikes. In addition, dynamic videos are also tested with simulated RGC spikes and with the pre-trained SID model from CAFAR10. The results show that our SID can decode natural scenes from both biological and modeled spike data with very good precision.

A. Decoding visual scenes from experimental data

Here the experimental data are a population of RGCs recorded from salamander retina [27] (see Methods), where the stimuli include static natural images and dynamic video, and the spike counts of the recorded RGCs are used as the input of our decoding model to reconstruct natural scenes.

1) *Decoding natural image stimulus*: For natural images, there are 300 images as stimulus and 80 RGCs showing spike responses. For the decoder, spike counts of 80 RGCs in response to each image are collected at one end, the other end is a training set of 270 images of 64×64 pixels each. For each image, spike-image converter up-sample a populating of 80 spike counts into an image with 64×64 pixels to get an intermediate image, which then is mapped to the target training image with the image-image autoencoder.

Fig. 2 shows the decoding results on some example testing images, where the global contents of images are reconstructed well while some details are missed. Final reconstructions are similar to each other viewed from our naked eyes, but there are some fine differences in the detailed

textures. Depending on the loss functions used for training, intermediate images can be very different. When there are two losses for each stage of the decoder as in \mathbf{L}_1 and \mathbf{L}_2 , the intermediate image (denoted as \mathbf{O}_1) is an preliminary image close to the target image. When there is one loss for both stages of the model as in \mathbf{L}_3 , the intermediate image is like noise without any visual structure.

Table I shows the performance of our model characterized by three typical measures of reconstructed images: mean square error (MSE) that describes the absolute difference of every pixel, peak signal to noise ratio (PSNR) that characterizes the global quality, and structural similarity index measure (SSIM) that captures the details or image distortion, for evaluating the reconstruction results. In general, all three loss functions give similar performances in terms of three measures. MSE and PSNR achieve the best results with \mathbf{L}_1 as both measures are correlated, while SSIM is the best with \mathbf{L}_2 . However, three measures are not perfect characteristics in the field of computer visions. For example, the reconstructed images with \mathbf{L}_2 look not good as the other two, however, it has the best SSIM measures. Therefore, three measures are a general guideline rather than the precise characteristic, as it seems that there is no perfect measure [30], [31].

2) *Decoding dynamic video stimulus*: So far, most of the decoding studies focus on static natural images, or some simple artificial dynamic scenes [13], [14]. To study dynamical visual scenes, such as videos with highly complex dynamics in both spatial and temporal domains, one has to, traditionally, understand how to deal with strong temporal adaptation observed in single neurons and neural circuits in the retina [24]. Here with the video stimulus containing 1800 frames of the size 64×64 each, and a population of 90 RGCs spike trains, our SID can overcome this difficulty with training of randomly selected frames out of the whole video, and testing on a subset untrained frames (see Methods).

From the reconstructed sample frames of test dataset shown in Fig. 3, one can see that our decoding model obtain high precise results, which can not only reconstruct the global content of each frame, but also some details of images that are missed in previous decoding studies [14], [16], [15].

The quantified performance is shown in Table I with the same measures. In contrast to image results, all three measures, MSE, PSNR, and SSIM, indicate that the best results are obtained with \mathbf{L}_3 . In addition, the performance with \mathbf{L}_3 is almost 50% higher than the other two losses. Such a good performance can also be seen from the sample images in Fig. 3 where both global

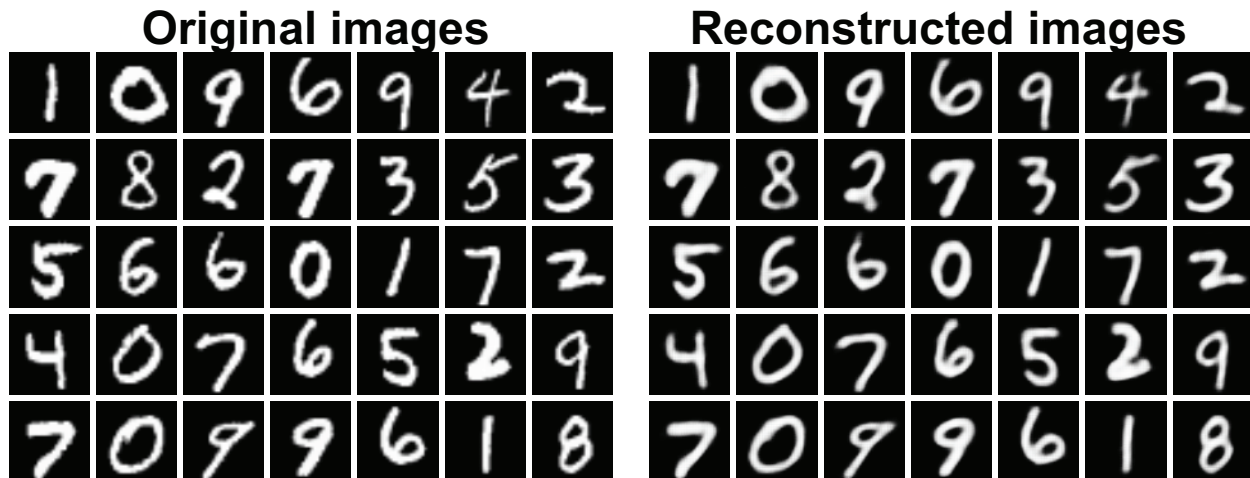


Fig. 4: Reconstructed example images of MNIST dataset. (Left) original images in test dataset. (Right) Reconstructed images from a population of simulated RGC spikes.

TABLE II: Quantified comparison to other decoding results of MNIST dataset based on fMRI data with different decoders. The compared values are taken from [19], where PSNR values are not provided. The last row is our results based on SID.

| Decoder | MSE | PSNR | SSIM |
|---------|--------------|---------------|--------------|
| [32] | 0.119 | - | 0.192 |
| [33] | 0.074 | - | 0.358 |
| [34] | 0.042 | - | 0.466 |
| [15] | 0.038 | - | 0.613 |
| [35] | 0.037 | - | 0.645 |
| [19] | 0.042 | - | 0.750 |
| Ours | 0.003 | 25.470 | 0.943 |

contents and fine details are clearly obtained.

B. Decoding visual scenes from simulated spikes

To further test the generalization capability of our decoding model, we did numerical experiments on simulated RGC data by creating a retinal encoding model based on the typical linear-nonlinear model and biological experimental data to simulate RGC responses (see Methods). In this way, one can simulate RGC spiking responses for any given stimuli. For comparison with experimental RGC data, we simulated the same number of 90 RGCs to obtain spikes.

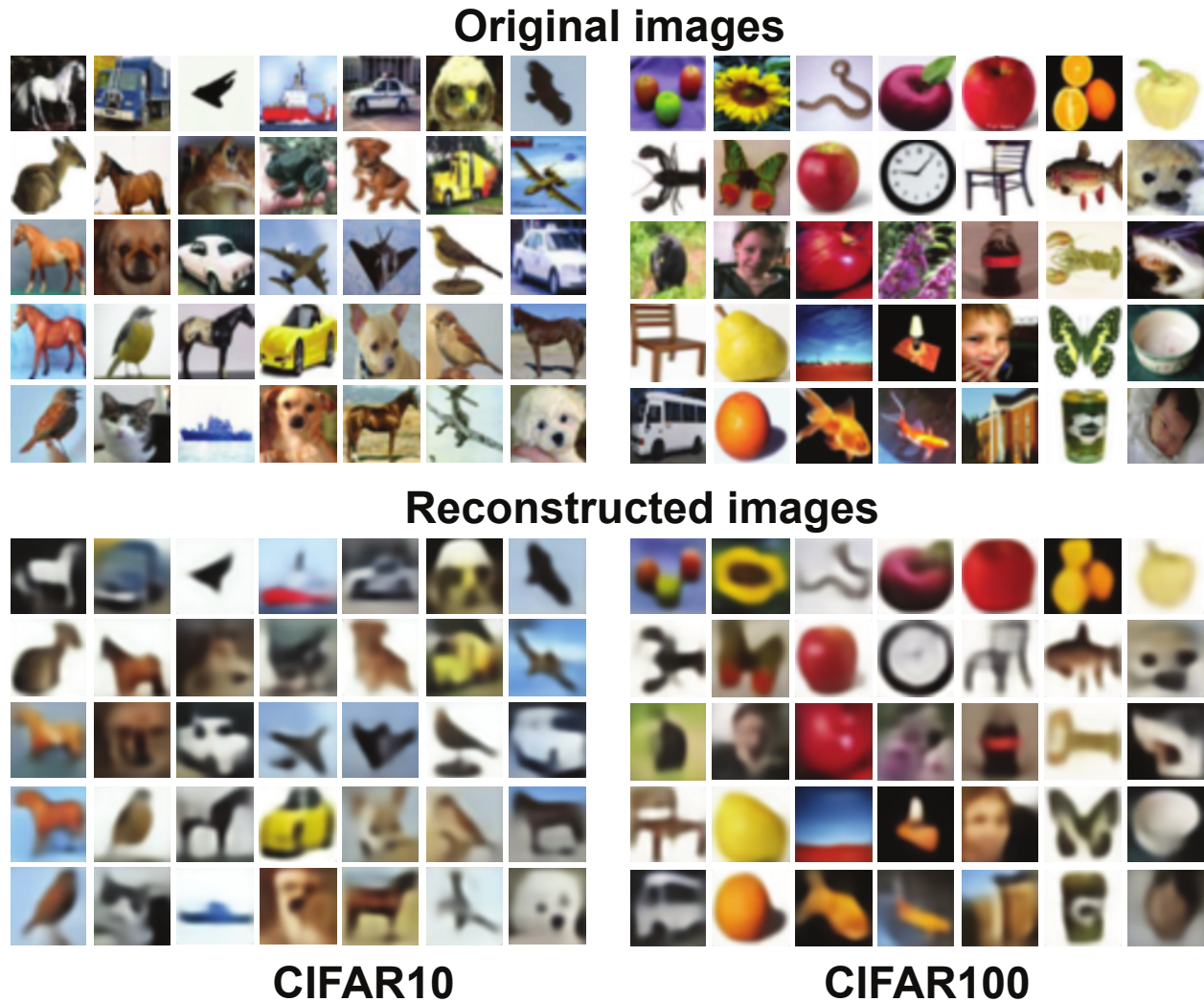


Fig. 5: Reconstructed example images from CIFAR10 (left) and CIFAR100 (right) datasets. (Top) original images in test set. (Bottom) Reconstructed images from simulated RGC spikes.

We first did experiments on the most popular image dataset, MNIST. A population of neural spikes was obtained for each image of MNIST with the encoding model. Then the SID was trained for the training set of MNIST, and tested on a separate test data. The MNIST reconstructed example images are shown in Fig. 4 with good quality, which can be characterized by the same measures of MSE, PSNR and SSIM listed in Tab. II. As there is no direct model so far based on neural spikes for MNIST, we compared our results with the decoding results based on the models developed for fMRI data [19]. Clearly, The SID is much better than these decoders, which are based on the similar decoding approaches of deep learning, although the target neural

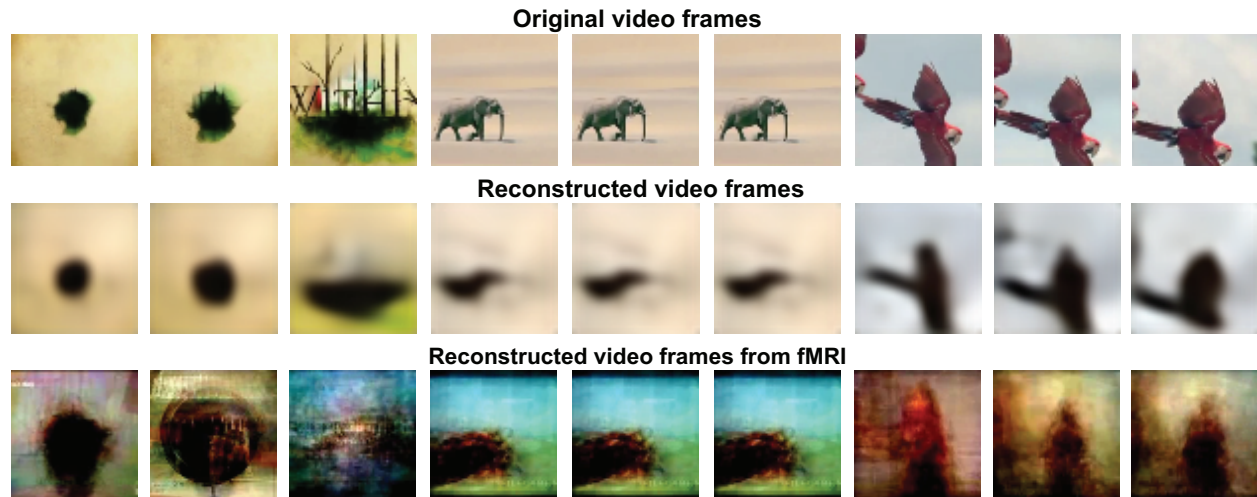


Fig. 6: Reconstructed dynamic videos with a pre-trained SID. (Top) original video frames from three segments of videos. (Middle) reconstructed video frames from simulated RGC spikes with a SID model pre-trained on CIFAR10 dataset. (Bottom) reconstructed video frames based on fMRI signals [16]

TABLE III: Quantified performance of reconstructed images measured by MSE, PSNR and SSIM for simulated RGC spikes with three different loss functions.

| Reconstruction | MSE | PSNR | SSIM |
|----------------|-------|--------|-------|
| Ours | 0.012 | 19.273 | 0.669 |
| [16] | 0.167 | 8.183 | 0.266 |

signal is fMRI data [32], [33], [34], [15], [35], [19].

Then we examined our model with two other popular image datasets, CIFAR10 and CIFAR100 by encoding them into RGC spike responses, then decoding simulated spikes to reconstruct stimulus images. The reconstructed sample images of the test set are shown in Fig. 4 for CIFAR 10 and CIFAR 100. All reconstructed images contain both global contents and fine details of stimulus images. For comparison with experimental RGC data, we only simulated the same number of 90 RGCs to obtain spikes, thus, the reconstructed images look a bit blurry. Yet, they show good performance already.

Next, we used the encoding model to simulated RGCs in response to dynamic videos. For comparison, the same set of videos used in [16] were encoding into RGC spikes by our model.

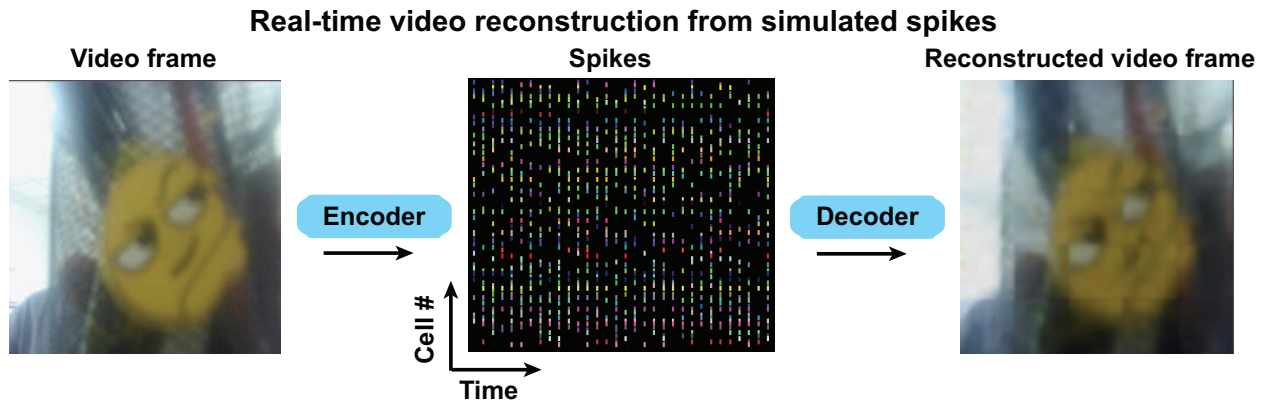


Fig. 7: Decoding of real-time video. (Left) One example frame of real-time video captured by a standard camera. (Middle) A population of spike trains obtained by the encoder. Each line represents one RGC’s spikes. (Right) The same frame reconstructed in a real-time fashion by the SID.

Then the SID model pre-trained with CIFAR10 was used to reconstruct the videos from simulated RGC spikes. As shown in Fig 6, the SID can reconstruct the dynamic videos from spikes very well. Compared with the fMRI decoded results [16], our reconstructed videos contain more semantic contents and are much more refined. What is more, the SID model used here is pre-trained with CIFAR10, which means that our SID model has a very great generalization capability for arbitrary visual scenes. The complete videos reconstructed are available online (see Methods).

Finally, based on the results above, we implemented a real-time artificial vision system (see Methods), where real-time videos are captured by a camera, then encoded into a population of neural spikes, which are fed into the SID to reconstruct the visual scenes. Fig. 7 shows a snapshot of real-time recorded video. Depending on the hardware, the speed and resolution of video can be greatly improved. For this real-time system, the SID is also pre-trained with the same CIFAR-10 dataset. These results suggest that our model can serve as a framework to deal with those artificial event-based vision [36].

IV. DISCUSSION

In this study, we proposed an end-to-end spike-image decoder to reconstruct stimulus images from neural spikes based on the retinal ganglion cells. The capability of SID was tested on experimental RGC data for both static and dynamic natural scenes to obtain state-of-the-art

reconstruction performance. Furthermore, by using an additional encoding model, the great performance of reconstruction of arbitrary visual scenes was demonstrated on popular image datasets. We also examined the generalization ability of SID by using a pre-trained SID to decode various types of dynamic videos to achieve real-time encoding and decoding visual scenes by neural spikes.

Our decoder can be thought as a general framework, in which the detailed network structures are flexible. Here we only explored the simple and perhaps the most basic structure, e.g., a simple dense connected and layered network for the spike-image converter and a typical autoencoder network for the image-image autoencoder. Given the rapid development of architecture design for artificial neural networks, it is possible to use other networks, such as those networks related to generative adversarial network [37] to further improve the decoding ability.

Recent experimental advancements in neuroscience can collect a large population of neurons simultaneously. In particular, in the retina, a population of spike trains from hundreds of retinal ganglion cells can be obtained with well-controlled visual scenes, such as images and movies [27], [14]. Together with other recent studies [21], [14], our results in this work show that a better decoding performance can be achieved with neural spikes, which is beyond the scope of fMRI signal [15]. Our study here provides a proof-of-principle of encoding and decoding visual scenes with only a small population of retinal neurons, which suggests that the performance of neuroprosthesis for restoring vision can be improved by the encoding/decoding algorithms besides of hardware design [38], [39], [40]. The benefit of decoding models is to justify the spiking patterns produced by the targeted downstream neurons, such that electrical stimulation should be able to close to those desired patterns of retinal neural activity in a prosthesis [41], [21], [38], which is beyond the traditional way of computing the distance between two or more spike trains in general [42], [43], [44].

The modelling framework mentioned in this paper could be used for other artificial visual systems. Visual scenes are highly complex with the information presented a spatiotemporal fashion and high-order correlations [2]. Recent advancements of computer vision make some breakthroughs for analyzing these complex natural scenes [45]. However, the efficiency, generalization ability, and adaption or transfer learning between different tasks, of well-trained models are still far from human performance [46]. Our model shows a great generalization ability for coding of visual scenes.

The main feature of these algorithms is to make use of neural spikes. Advancements of

recent artificial intelligence computing align with the development of the next generation of neuromorphic chips and devices, where the new data format is processed spikes or events [47], [48], [36]. Therefore, the methods can be applied for neuromorphic visual cameras with spike or event signals as well. Taken together with neuromorphic hardware and event/spiking computing algorithm, the next generation of computational vision can develop a better system for artificial vision.

REFERENCES

- [1] D. C. Knill and A. Pouget, "The bayesian brain: the role of uncertainty in neural coding and computation," *Trends in Neurosciences*, vol. 27, no. 12, pp. 712–9, 2004.
- [2] E. P. Simoncelli and B. A. Olshausen, "Natural image statistics and neural representation," *Annual Review of Neuroscience*, vol. 24, no. 24, p. 1193, 2001.
- [3] M. C.-K. Wu, S. V. David, and J. L. Gallant, "Complete functional characterization of sensory neurons by system identification," *Annual review of neuroscience*, vol. 29, pp. 477–505, 2006.
- [4] P. D. Jazdzinsky and S. A. Baccus, "Transformation of visual signals by inhibitory interneurons in retinal circuits," *Annual Review of Neuroscience*, vol. 36, pp. 403–28, 2013.
- [5] T. Euler, S. Haverkamp, T. Schubert, and T. Baden, "Retinal bipolar cells: elementary building blocks of vision," *Nature Reviews Neuroscience*, vol. 15, no. 8, p. 507, 2014.
- [6] S. A. Bloomfield and B. Völgyi, "The diverse functional roles and regulation of neuronal gap junctions in the retina," *Nature Reviews Neuroscience*, vol. 10, no. 7, p. 495, 2009.
- [7] W. N. Grimes, A. Songco-Aguas, and F. Rieke, "Parallel processing of rod and cone signals: Retinal function and human perception," *Annual Review of Vision Science*, vol. 4, pp. 123–141, 2018.
- [8] J. O'Brien and S. A. Bloomfield, "Plasticity of retinal gap junctions: Roles in synaptic physiology and disease," *Annual Review of Vision Science*, vol. 4, pp. 79–100, 2018.
- [9] M. Rivlin-Etzion, W. N. Grimes, and F. Rieke, "Flexible neural hardware supports dynamic computations in retina," *Trends in Neurosciences*, vol. 41, pp. 224–237, 2018.
- [10] J. B. Demb and J. H. Singer, "Functional circuitry of the retina," *Annual Review of Vision Science*, vol. 1, pp. 263–289, 2015.
- [11] T. Gollisch and M. Meister, "Eye smarter than scientists believed: Neural computations in circuits of the retina," *Neuron*, vol. 65, no. 2, pp. 150–164, jan 2010.
- [12] A. F. Meyer, R. S. Williamson, J. F. Linden, and M. Sahani, "Models of neuronal stimulus-response functions: elaboration, estimation, and evaluation," *Frontiers in systems neuroscience*, vol. 10, p. 109, 2017.
- [13] T. Gollisch and M. Meister, "Rapid neural coding in the retina with relative spike latencies," *Science*, vol. 319, no. 5866, pp. 1108–11, 2008.
- [14] V. Botella-Soler, S. Deny, G. Martius, O. Marre, and G. Tkačik, "Nonlinear decoding of a complex movie from the mammalian retina," *PLoS Computational Biology*, vol. 14, no. 5, p. e1006057, 2018.
- [15] H. Wen, J. Shi, Y. Zhang, K.-H. Lu, J. Cao, and Z. Liu, "Neural encoding and decoding with deep learning for dynamic natural vision," *Cerebral cortex*, vol. 28 12, pp. 4136–4160, 2018.
- [16] S. Nishimoto, A. T. Vu, T. Naselaris, Y. Benjamini, B. Yu, and J. L. Gallant, "Reconstructing visual experiences from brain activity evoked by natural movies," *Current Biology*, vol. 21, no. 19, pp. 1641–1646, 2011.

- [17] B. Thirion, E. Duchesnay, E. Hubbard, J. Dubois, J.-B. Poline, D. LeBihan, and S. Dehaene, “Inverse retinotopy: inferring the visual content of images from brain activation patterns,” *Neuroimage*, vol. 33, no. 4, pp. 1104–1116, 2006.
- [18] T. Naselaris, R. J. Prenger, K. N. Kay, M. Oliver, and J. L. Gallant, “Bayesian reconstruction of natural images from human brain activity,” *Neuron*, vol. 63, no. 6, pp. 902–915, 2009.
- [19] K. Qiao, C. Zhang, L. Wang, J. Chen, L. Zeng, L. Tong, and B. Yan, “Accurate reconstruction of image stimuli from human functional magnetic resonance imaging based on the decoding model with capsule network architecture,” *Front Neuroinform*, vol. 12, p. 62, 2018.
- [20] O. Marre, V. Botella-Soler, K. D. Simmons, T. Mora, G. Tkačik, and M. J. Berry II, “High accuracy decoding of dynamical motion from a large retinal population,” *PLoS Computational Biology*, vol. 11, no. 7, p. e1004304, 2015.
- [21] N. Parthasarathy, E. Batty, W. Falcon, T. Rutten, M. Rajpal, E. Chichilnisky, and L. Paninski, “Neural networks for efficient bayesian decoding of natural images from retinal neurons,” in *Advances in Neural Information Processing Systems 30*, I. Guyon, U. V. Luxburg, S. Bengio, H. Wallach, R. Fergus, S. Vishwanathan, and R. Garnett, Eds. Curran Associates, Inc., 2017, pp. 6437–6448.
- [22] G. B. Stanley, F. F. Li, and Y. Dan, “Reconstruction of natural scenes from ensemble responses in the lateral geniculate nucleus,” *Journal of Neurophysiology*, vol. 19, no. 18, pp. 8036–8042, 1999.
- [23] S. Garasto, A. A. Bharath, and S. R. Schultz, “Visual reconstruction from 2-photon calcium imaging suggests linear readout properties of neurons in mouse primary visual cortex,” *bioRxiv*, p. 300392, 2018.
- [24] J. K. Liu and T. Gollisch, “Spike-triggered covariance analysis reveals phenomenological diversity of contrast adaptation in the retina,” *PLoS Computational Biology*, vol. 11, no. 7, p. e1004425, jul 2015.
- [25] Y. Yue, L. He, G. He, J. Liu, K. Du, Y. Tian, T. Huang *et al.*, “A simple blind-denoising filter inspired by electrically coupled photoreceptors in the retina,” *arXiv preprint arXiv:1806.05882*, 2018.
- [26] M. D. Zeiler and R. Fergus, “Visualizing and understanding convolutional networks,” in *European Conference on Computer Vision*, 2014, pp. 818–833.
- [27] A. Onken, J. K. Liu, P. C. R. Karunasekara, I. Delis, T. Gollisch, and S. Panzeri, “Using matrix and tensor factorizations for the single-trial analysis of population spike trains,” *PLoS Computational Biology*, vol. 12, no. 11, p. e1005189, nov 2016.
- [28] J. K. Liu, H. M. Schreyer, A. Onken, F. Rozenblit, M. H. Khani, V. Krishnamoorthy, S. Panzeri, and T. Gollisch, “Inference of neuronal functional circuitry with spike-triggered non-negative matrix factorization,” *Nature Communications*, vol. 8, no. 1, p. 149, jul 2017.
- [29] E. J. Chichilnisky, “A simple white noise analysis of neuronal light responses,” *Network*, vol. 12, no. 2, pp. 199–213, 2001.
- [30] A. Hore and D. Ziou, “Image quality metrics: Psnr vs. ssim,” 08 2010, pp. 2366–2369.
- [31] Z. Wang, E. P. Simoncelli, and A. C. Bovik, “The thirty-seventh asilomar conference on signals, systems computers, 2003,” vol. 2, Nov 2003, pp. 1398–1402 Vol.2.
- [32] Y. Fujiwara, Y. Miyawaki, and Y. Kamitani, “Modular encoding and decoding models derived from bayesian canonical correlation analysis,” *Neural computation*, vol. 25, no. 4, pp. 979–1005, 2013.
- [33] W. Wang, R. Arora, K. Livescu, and J. Bilmes, “On deep multi-view representation learning,” pp. 1083–1092, 2015.
- [34] Y. Miyawaki, H. Uchida, O. Yamashita, M. aki Sato, Y. Morito, H. C. Tanabe, N. Sadato, and Y. Kamitani, “Visual image reconstruction from human brain activity using a combination of multiscale local image decoders,” *Neuron*, vol. 60, pp. 915–929, 2008.
- [35] C. Du, C. Du, and H. He, “Sharing deep generative representation for perceived image reconstruction from human brain activity,” pp. 1049–1056, 2017.

- [36] G. Gallego, T. Delbruck, G. Orchard, C. Bartolozzi, B. Taba, A. Censi, S. Leutenegger, A. Davison, J. Conradt, K. Daniilidis, and D. Scaramuzza, “Event-based vision: A survey,” *arXiv preprint arXiv:1904.08405*, 2019.
- [37] I. Goodfellow, J. Pouget-Abadie, M. Mirza, B. Xu, D. Warde-Farley, S. Ozair, A. Courville, and Y. Bengio, “Generative adversarial networks,” *Advances in Neural Information Processing Systems*, vol. 3, 06 2014.
- [38] S. Nirenberg and C. Pandarinath, “Retinal prosthetic strategy with the capacity to restore normal vision,” *Proceedings of the National Academy of Sciences*, vol. 109, no. 37, pp. 15 012–15 017, aug 2012.
- [39] L. Yue, J. D. Weiland, B. Roska, and M. S. Humayun, “Retinal stimulation strategies to restore vision: Fundamentals and systems,” *Progress in retinal and eye research*, vol. 53, pp. 21–47, 2016.
- [40] B. Yan and S. Nirenberg, “An embedded real-time processing platform for optogenetic neuroprosthetic applications,” *IEEE transactions on neural systems and rehabilitation engineering: a publication of the IEEE Engineering in Medicine and Biology Society*, vol. 26, no. 1, pp. 233–243, 2018.
- [41] Z. Li, “Decoding methods for neural prostheses: where have we reached?” *Frontiers in systems neuroscience*, vol. 8, p. 129, 2014.
- [42] J. D. Victor, “Spike train metrics,” *Current opinion in neurobiology*, vol. 15, no. 5, pp. 585–592, 2005.
- [43] M. v. Rossum, “A novel spike distance,” *Neural computation*, vol. 13, no. 4, pp. 751–763, 2001.
- [44] N. P. Shah, S. Madugula, E. Chichilnisky, J. Shlens, and Y. Singer, “Learning a neural response metric for retinal prosthesis,” *bioRxiv*, p. 226530, 2017.
- [45] Y. Lecun, Y. Bengio, and G. Hinton, “Deep learning,” *Nature*, vol. 521, no. 7553, pp. 436–444, 2015.
- [46] A. H. Marblestone, G. Wayne, and K. P. Kording, “Toward an integration of deep learning and neuroscience,” *Frontiers in Computational Neuroscience*, vol. 10, p. 94, sep 2016.
- [47] S. Dong, T. Huang, and Y. Tian, “Spike camera and its coding methods,” in *Data Compression Conference (DCC), 2017*. IEEE, 2017, pp. 437–437.
- [48] Z. Bi, S. Dong, Y. Tian, and T. Huang, “Spike coding for dynamic vision sensors,” in *2018 Data Compression Conference*. IEEE, 2018, pp. 117–126.